Experimental Investigation of the Jets in Crossflow: Nonswirling Flow Case

A. Strzelecki* and P. Gajan
ONERA-Centre de Toulouse, 31055 Toulouse, France
L. Gicquel[†]
European Centre for Research and Advanced Training in Scientific Computation,
31057 Toulouse, France
and
B. Michel*
ONERA-Centre de Toulouse, 31055 Toulouse, France

The mixing of eight isothermal jets issuing in a fully developed circular pipe flow is investigated by means of laser Doppler anemometry, particle image velocimetry, and planar laser induced fluorescence techniques. Two values of the momentum ratio are considered. Unsteady and steady flow patterns are analyzed. Characteristic frequencies are deduced from spectral analysis. Velocity and scalar concentration fields are compared. The mean centerline concentration decay is characterized. The analysis of the flow instabilities is focused on the wake-type structures downstream of the jets and the shear layer structures appearing between the jet and the main flow. The results on the wake-type structures are consistent with previous observations done on a single jet. In particular, the influence of the velocity ratio on the signal-to-noise ratio is confirmed. The Strouhal number associated with the shear layer structure depends on the velocity ratio and on the Reynolds number. The comparison between the velocity and concentration fields confirms the difference in the jet trajectories deduced from these two fields. The detailed analysis of the concentration field gives useful information on the influence of the confinement on the jets' behavior.

Nomenclature

b	=	distance from the maximum concentration location where $C(x, b) = 0.5C_{\max}(x)$, m
b_{in}	=	b value toward the wall, m
b_{out}	=	b value toward the pipe axis
$C(x, y, z)$	=	concentration
$C_{\max}(x)$	=	maximum concentration value in the section
D	=	pipe diameter, m
d	=	jet diameter, m
J	=	momentum flux ratio $(= (\rho_{\text{jet}} U_{\text{jet}}^2)/(\rho_o U_o^2))$
k	=	kinetic turbulence level, $(\text{m/s})^2$
$Q_{m_{\text{axial}}}$	=	mass flow rate of the crossflow, kg/m^3
$Q_{m_{\text{jets}}}$	=	mass flow rate of the jet flow, kg/m^3
R	=	jet-to-crossflow-velocity ratio $(= U_{\text{jet}}/U_o)$
(r, θ, x)	=	polar coordinate
Re_{jets}	=	Reynolds number calculated from the jet diameter and the jet bulk velocity
Re_o	=	Reynolds number calculated from the pipe diameter and the upstream bulk velocity
s	=	spatial coordinate along the jet trajectory, m
St_j	=	Strouhal number calculated from the jet diameter and the jet bulk velocity
St_o	=	Strouhal number calculated from the jet diameter and the upstream bulk velocity
U_{jets}	=	jet bulk velocity, m/s
U_o	=	main flow bulk velocity, m/s
(x, y, z)	=	Cartesian coordinate
$y_{\max}$	=	distance from the wall where $C_{\max}(x)$ is reached

*2 Avenue Edouard Belin.
†42 Avenue Gaspard Coriolis.

Introduction

CURRENT demands to optimize combustion performance and reduce pollutant emissions require considerable research efforts from the gas turbine industry. The basic objectives in combustor design are to achieve easy ignition, high combustion efficiency, and minimum pollutant emissions. In this context, numerical methods are very attractive alternatives to the expensive experimental setups required in these areas of research. In the last decade, experimental and numerical studies have indicated that unsteady phenomena play an important role in fuel injection, combustion processes, and flow mixing [1]. Contrary to the Reynolds-averaged Navier–Stokes (RANS) equations, which are restricted to steady turbulent flows, LES (large-eddy simulations) or URANS (unsteady Reynolds-averaged Navier–Stokes) simulations reproduce flow unsteadiness in such a way as to obtain a better prediction of combustion efficiency or combustion instabilities. Nevertheless, in order to develop such numerical tools, it is necessary to validate them on flow conditions reproducing unsteady phenomena observed in actual combustion chambers. This is the case in the dilution zone where an array of "cold" jets issues transversally into a main hot flow coming from the combustion region. In this zone, large-scale structures control the effectiveness and the efficiency of the mixing.

The mixing of a transverse jet in a nonconfined environment has been studied for more than 60 years ([2–21]). A detailed description of this work may be found in Margason [2] and Smith and Mungal [7]. Analyses of vortical structures were performed and correlations were deduced from velocity or scalar concentration fields in order to calculate the jet trajectory from geometrical and flow parameters. In particular, the role of the momentum flux ratio J was highlighted. Some publications also deal with the mixing of multiple jets in a confined crossflow ([11–15]). The influences of different geometrical parameters (spacing between jets S, size and shape of the holes, distribution of the holes on the wall surface, and height of the channel H) were analyzed. For a rectangular channel with a height H, Holdeman [11] observed that the jet penetration depends on a parameter Γ equal to $(S/H)\sqrt{J}$. For circular pipes this parameter is equal to $\pi\sqrt{2J}/n$ with n the number of holes (Holdeman

et al. [12]). Optimum values of this parameter were obtained in order to enhance the mixing between the jets and the main flow. For a cylindrical pipe and a single row of circular orifices, Leong et al. [13] suggested that the optimal mixing is obtained for $\Gamma = 2.5$. Leong et al. [13] observed that for given momentum and mass ratios the jet penetration decreases as the jet spacing diminishes.

This paper deals with isothermal jets in crossflow. It includes a comparison between previous works and the results of recent experiments. To reproduce the dynamics of the actual flow appearing in a dilution zone of a combustor chamber and obtain a detailed database, an experimental setup, consisting of eight transverse jets flowing into a pipe flow, was defined. Optical techniques [laser Doppler anemometry (LDA), particle image velocimetry (PIV), and planar laser induced fluorescence (PLIF)], and spectral analyses were applied in order to obtain a detailed description of the mean and unsteady characteristics of the flow. In parallel, LES simulations with the AVBP code of the European Centre for Research and Advanced Training in Scientific Computation were performed and compared with the experimental results. This comparison with the LES calculations was published in Prière et al. [15].

Experimental Setup, Measurement Techniques, and Flow Conditions

This section shows the experimental setup, measurement techniques, and flow > conditions used in the experiments.

Experimental Setup

The test rig used for this study is shown in Fig. 1. The total mass airflow rate issuing from a high-pressure tank (70 bars) is measured by a sonic nozzle with an accuracy of 0.9%. The flow then divides into an axial flow and a series of jet flows, which have respective flow rates of $Q_{m_{axial}}$ and $Q_{m_{jets}}$. The jets' mass flow rate is determined by means of a turbine flow meter with an accuracy of 1%. A sketch of the test section with the main dimensions is presented in Fig. 2.

It is designed for optical measurements. The 100 mm internal diameter (D) tube and the lateral windows are made of Suprasil glass in order to permit UV lighting for PLIF measurements. Eight circular orifices with diameters d equal to 6.1 mm are drilled in the glass wall in the same cross section at different θ values (0, 45, 90, 135, 180, 225, 270, and 315°, respectively). These holes converge slightly in order to ensure a flat velocity profile at the jet exits. The radius of curvature of these contractions is equal to 4.25 mm and the contraction ratio is equal to 0.811. The thickness of the glass tube is 1.5 mm. The secondary flow arrives in a settling chamber through four entrances before penetrating transversally into the main flow through the eight orifices. This chamber is divided in two parts separated by a grid having a porosity of 0.2 in order to homogenize the flow rate distribution and to lower the turbulence levels upstream of the jet entrances. The total length and volume of this chamber are equal to 0.31 m and 3.8×10^{-3} m^3, respectively. The differential pressure occurring between the settling chamber and the pipe controls the jet velocity.

Experimental Techniques

During these experiments, four experimental techniques were applied. In a first step a 2-D LDA system was used in order to obtain a detailed description of averaged velocity and turbulence fields $10d$ in four pipe sections located upstream ($-0.3d$) and downstream of the jet exits (2, 5, and 10d). The size of the measurement volume is equal to 1.3 mm in length and 90 μm in diameter. The flow is seeded with droplets of olive oil. Measurements are performed on 18 radiuses as shown in Fig. 3a. On each radius, 50 points are considered. To determine the three velocity components, we suppose that the boundary conditions are the same for each jet. By comparing the measurements obtained on two orthogonal jets, the velocity and turbulence field can be determined (Fig. 3b).

PIV and PLIF techniques are used to study the large structure and the mixing induced downstream of the jet outlets. In these two cases, two types of measurement are taken [cross view and longitudinal
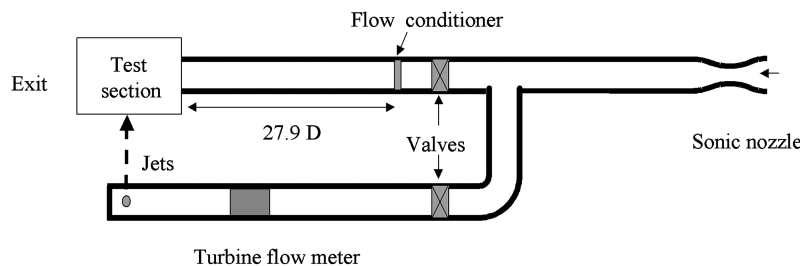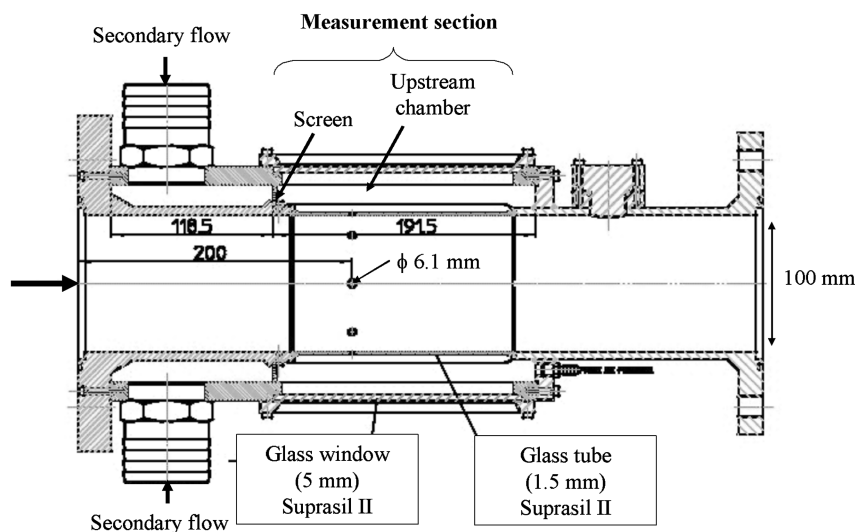

Fig. 1   Experimental set up.
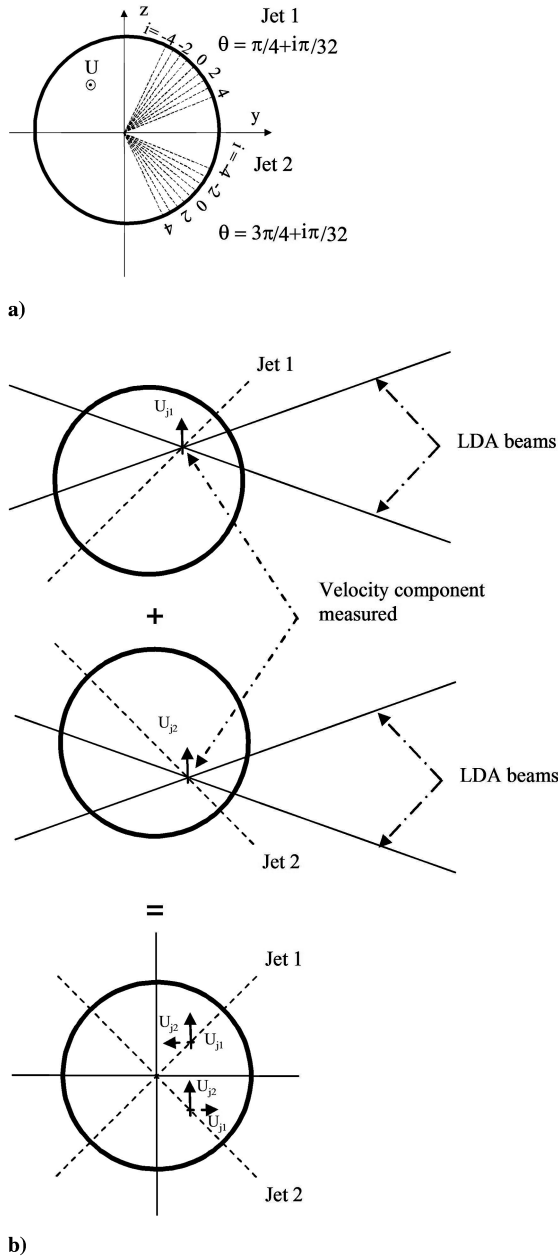

Fig. 2   Sketch of the test section.

a)

b)

Fig. 3   LDA Measurements showing a) mesh, and b) the method used to achieve the three velocity components from a 2-D system.
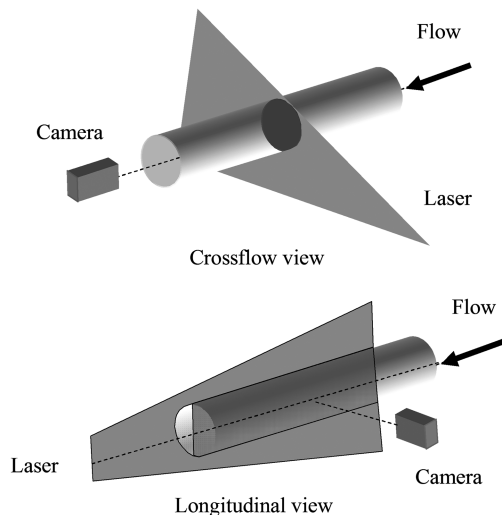

Crossflow view

Longitudinal view

Fig. 4   Optical arrangement for the PIV and PLIF measurements.

view (Fig. 4)]. The transverse flow is analyzed in different pipe sections downstream of the jet exits (0, 2, 5, and 10d). The laser sheet is orthogonal to the pipe axis and the camera is placed in front of the open section of the pipe. The scene observed corresponds to the entire cross section. A close-up of the exit of one jet is considered in order to define the inlet conditions for the jet flow. For longitudinal views, the respective positions of the laser sheet and the camera are permutated. The flow is seeded with glycol droplets injected upstream of the test section. For PIV measurements both flows are seeded. For visualizations the glycol droplets are only injected in the jet flow. The particles are illuminated by a laser sheet using a laser Quanta_Ray Nd:Yag from Spectra Physics. The CCD (charge-coupled devide) video camera SharpVISION 1300-DE has a spatial resolution of 1300 (H) × 1030 (V). Two camera lenses with different focal lengths are used (60 and 210 mm, respectively). The acquisition rate is equal to 3 Hz. At each time step, two successive frames are acquired. The interframe times can be as short as 200 ns. The images are acquired on a PC equipped with a video acquisition card. This also allows synchronization of the different systems used. The images of the particles are recorded and postprocessed. Details of how they are processed can be found in Lourenço and Krothapalli [22]. For each field, 250 pairs of images are acquired. Uncertainty in velocity measurements is generally caused by the seeding particle size, nonuniform particle distribution, displacement gradients, interrogation window size, and electronic and optical image noise (Raffel et al. [23]). The parameters used during the tests are summarized in Table 1. The velocity resolution is calculated from the spatial resolution of the images σ_I (m/pixel), the time interval between the two light pulses $\Delta t(s)$, and the number of instantaneous fields treated N. The smallest displacement detectable on one instantaneous field is equal 0.1 pixel and the smallest velocity measurable is equal to

$$U_{\min} = \frac{\sigma_I}{10 \cdot \Delta t}$$

Statistically, the interval confidence on the averaged velocity deduced from N samples is

$$\sigma_U = \frac{U_{\min}}{2\sqrt{N}}$$

The accuracy linked to the calibration is generally better than 0.8%.

The PLIF technique uses a monochromatic light source that is formed into a sheet and passed through the flowfield. The light source excites an energy transition in a marker species, which fluoresces upon relaxation [24]. The fluorescence is captured on an imaging array. In this study, acetone vapor is used as a tracer. Acetone fluorescence is a linear function of both incident laser energy and acetone concentration. Acetone absorbs in UV light (225–320 nm, 278 nm peak) and emits in the visible spectrum (350–550 nm, 435 peak) allowing for the use of CCD arrays. A quadrupled Nd YAG Spectra Physics laser provides a 90 mJ, 266 nm pulse, which is formed into a sheet and focused to a waist in the test section. The sheet thickness varied from 0.3 to 1.1 mm in the measured flowfield regions. Two lens arrangements are used to form either a parallel or a diverging laser sheet. Saturated acetone vapor is obtained by bubbling filtered air through two pressurized cylinders. This acetone-saturated air flow is then mixed with fresh air to form the jets' flow. The molar fraction of the final mixture is calculated from the pressure and the temperature in the tanks and the flow rates of the seeded and unseeded air flows. Typical concentrations of 4% are used during the experiments. A 1280 × 1024 pixel CCD camera FlowMaster3 captures the fluorescence. As the sensitivity of the camera is not sufficient to image the fluorescent field, the incoming light is first amplified by an intensifier. Two lenses with different focal lengths are used (105 and 210 mm, respectively) with an aperture of 5.6. For the smaller focal length used on the longitudinal visualization, the theoretical spatial resolution of the camera is equal to 63 μm/pixel. For each test, 100 images are recorded. Postprocessing is applied to eliminate the background. The background image is obtained by illuminating the scene with the laser sheet without flow. This

Table 1 Details of the PIV parameters used during the tests

Measurement type	View size, mm × mm	Averaged mesh size, mm × mm	Pixel resolution, μm	Δt, μs	σ_U, m/s
Transverse view					
Close-up $x/d = 0$ $R = 2$	20 × 16	0.26 × 0.26	17	1.05	0.2
Close-up $x/d = 0$ $R = 4$	43 × 34	0.47 × 0.47	34	1.5	0.26
Full pipe, $R = 2$					
2d	158 × 126	4.7 × 4.7	123	9.5	0.16
5d	154 × 123	1.7 × 1.7	120	9.5	0.16
10d	150 × 120	1.2 × 1.2	117	10	0.14
Full pipe, $R = 4$					
0d	158 × 126	7.7 × 7.7	123	6	0.24
0.67d	158 × 126	7.7 × 7.7	123	6	0.24
1.33d	158 ∗ 126	3 × 3	123	5	0.28
2d	158 × 126	1.8 × 1.8	123	7.5	0.20
5d	154 × 123	1.2 × 1.2	120	6	0.24
10d	150 × 120	1.2 × 1.2	117	12	0.12
Longitudinal view					
$R = 2$	64 × 51	0.64 × 0.64	50	1.05	0.6
$R = 4$	64 × 51	0.64 × 0.64	50	1.05	0.6

procedure permits one to eliminate both the noise of the camera and the laser reflections on the glass wall. On the longitudinal views the concentration is calculated using a linear law giving a concentration of 100% in the potential zone of the jets and 0% in the pipe section located upstream of the jet entrance. For cross views that do not visualize the potential region of the jets, the concentration levels are calculated by comparing the profiles obtained on longitudinal and transverse views. In the dilution zone, the molar fraction of acetone vapor in the jets is low enough to neglect the absorption effect on the laser sheet intensity. On cross-view images, a diopter effect and the internal reflections on the glass wall do not permit one to perform accurate corrections of the images. Nevertheless, a correction is applied on each image in order to take into account the spreading of the sheet. This correction is based on a comparison of the concentration fields measured on the eight jets. Only qualitative uses of these cross-view images are considered in this paper.

To evaluate the performance of the optical techniques used (PIV or PLIF), it is interesting to compare their spatial resolutions to the characteristic scales of turbulence or concentration. In a first approximation, we can estimate that the integral scale L is of the order of the jets orifices (6 mm). The Kolmogorov scale η is approximately equal to $L.Re_L^{-0.75}$. Thus, this length varies from 2 μm for the higher jet velocity to 10 μm for the lower. Following Batchelor [25,26], the smallest scale of concentration fluctuation is equal to $\eta(Sc)^{-0.5}$ where Sc is the Schmidt number. For the acetone, the Schmidt number is around one, and this new scale is of the same order as the Kolmogorov scale. From these calculations, we observe that only the largest scales of concentration and turbulence can be studied with the experimental set up used in this study.

To complete this database, spectral analyses were performed from velocity signals delivered by a hot-wire device. A DANTEC P11 probe with a typical length equal to 1.5 mm is used. The averaged spectrum is directly calculated with a Brüel and Kjær Analyzer 2032 from 1000 instantaneous spectra.

Flow Conditions

Previous studies indicate that jet behavior is mainly influenced by the momentum flux ratio J between the jet and the main flow. For equidensity flows, the velocity ratio R can be used. Two values of this parameter were considered ($R = 2$ and 4). The bulk velocity U_o is fixed at 25 m/s for LDA and PIV measurements. The characteristic Reynolds numbers are $Re_o = 1.7 \times 10^5$ and $Re_{jets} = 4.1 \times 10^4$ and 2.0×10^4, respectively. For PLIF it was lowered to 5 m/s due to seeding constraints. Note that, for a fixed value of the R ratio (=10), Smith and Mungal [7] observe no influence in the Reynolds number ($8.4 \times 10^3 < Re_{jets} < 3.3 \times 10^4$). In our case the pipe Reynolds number may affect the upstream velocity profile, which is not the case in the Smith and Mungal study. The change of the jet fluid density resulting from the acetone is not taken into

account. Note that the molar fraction in the jets is equal to 4%, which induces a density change of 4%.

For the spectral analyses, the jets Reynolds number Re_{jets} varies from 2.4×10^4 to 4.1×10^4 for the $R = 4$ case and from 1.0×10^4 to 2.2×10^4 for the $R = 2$ case.

The boundary conditions concern the main flow and the jet flows. The first are determined using LDA. They correspond to a fully developed pipe flow (Fig. 5). The boundary conditions for the jets are obtained from PIV measurements (Fig. 6). For $R = 4$ the profile is flat. For $R = 2$ the profiles measured 2 mm from the wall are asymmetrical.

Results and Discussion

Analysis of Flow Instabilities

The different observations obtained from flow visualizations show that the interaction between a jet and the main flow induces the formation of different categories of vortical structures (Werlé, [4], Fric and Roshko [5]). Four of these were observed (Fig. 7).

The shear layer vortices and the wake structures are intrinsically unsteady whereas the two others are basically steady even if they can have nonsteady components. Horseshoe structures are observed in laminar flow cases. As far as we know, the existence of such structures has not been proved in turbulent flow cases.

Mie flow visualizations of the shear layer structures are presented in Figs. 8 and 9. The vortices are due to Kelvin–Helmhotz instabilities between the jet and the main flow. They appear on the upstream and lee sides of the jet but also on lateral sides of the jet (Fig. 8). Lim et al. [9] gave a detailed description of the mechanisms
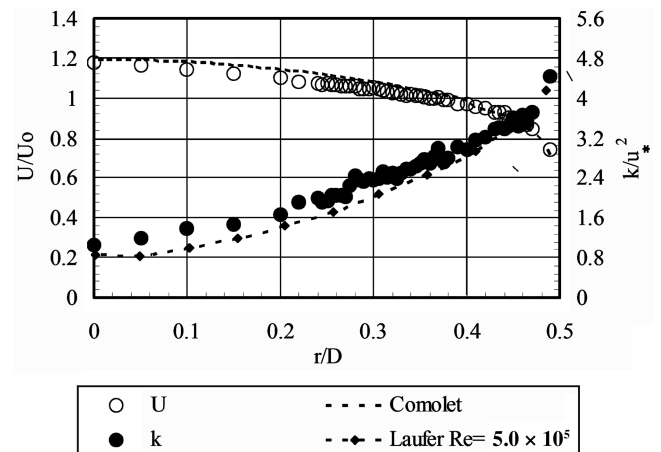

Fig. 5 Mean and turbulence profiles measured in the pipe upstream of the jet exit.
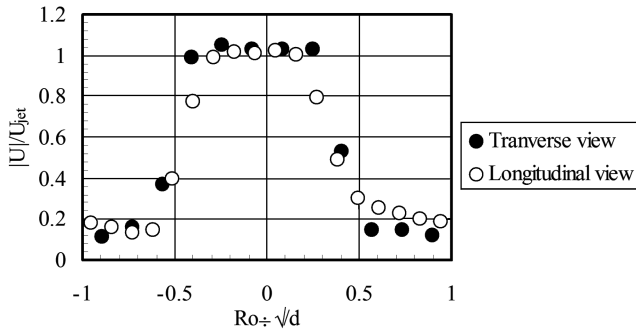
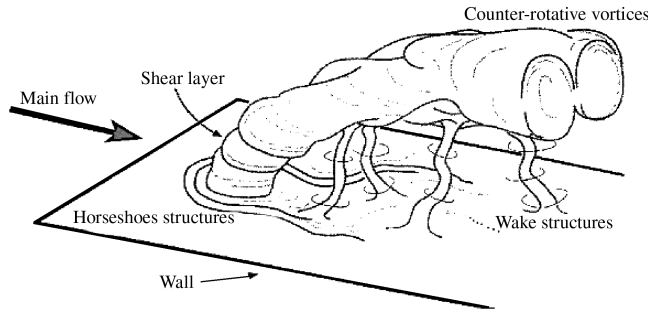**Fig. 6 Jet velocity profile measured by PIV (R = 4).**

Fig. 7 Instantaneous flow observed in a jet in crossflow (Fric and Roshko [5]).

of the loop vortices formations on the upstream and lee sides of the jet and their interaction with the counter-rotating vortices. The model proposed by Lim et al. contradicts previous hypotheses, which supposed that the loop vortices originate from vortex rings. The structures appearing on the lateral side can be interpreted as the arms of the loop vortices formed upstream of the jet. For the two velocity ratios considered, these structures are observed on both sides of the jet. Nevertheless, due to the asymmetry of the shearing and the formation of the two contra-rotating vortices, these loop vortices evolve rapidly, and only the upstream structures remain. If we compare the set of images obtained for the two R ratios (Fig. 9), it seems that the first rolling up appears closer to the wall when the R ratio diminishes. On the longitudinal views, a flapping movement of the jet exists after the zone of maximum deflection.

It is possible to characterize these different phenomena through a Strouhal number ($St_j = f \cdot d/U_{jet}$) based on the bulk velocity of the
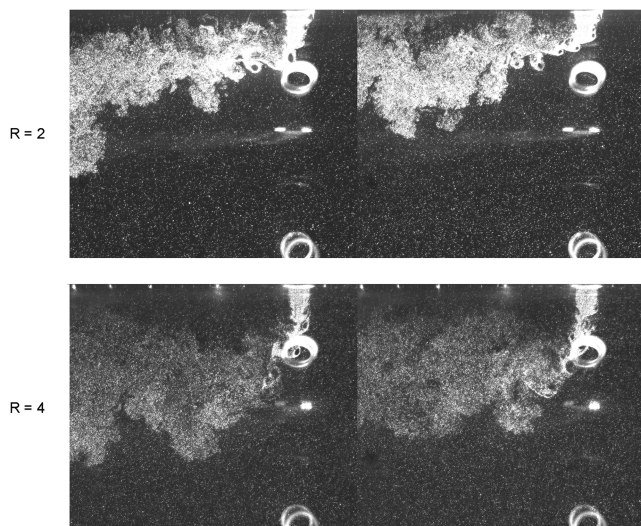

Fig. 8 Flow visualization of the shear layer structures (longitudinal view).
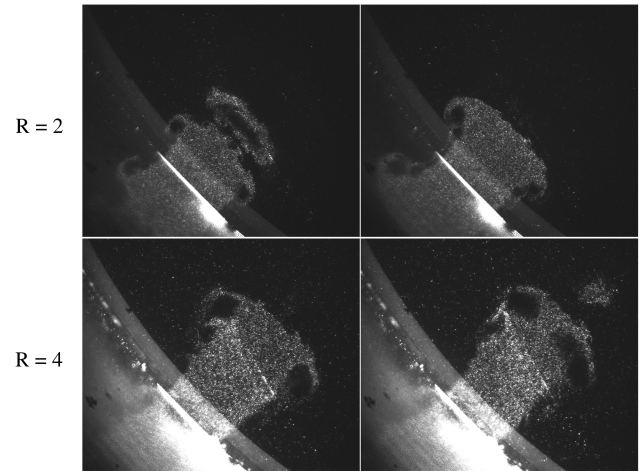

Fig. 9 Shear layer structures on the lateral boundaries of the jet (x/d = 0).

jet flow and the jet diameter. Kelso et al. [6] found that for $R = 2.2$ and a Reynolds number based on the jet velocity equal to 1.4×10^4, the Strouhal number is equal to 0.29. More recently, Megerian and Karagozian [16] and Megerian et al. [17] performed an experimental study in order to quantify and compare the preferred and shear layer modes of instability in the free jet and the transverse jet for jet Reynolds numbers between 1.7×10^3 and 3.0×10^3 and R ratio between 1.15 and infinity. Dominant instability modes are observed to move closer to the jet orifice as the R ratio is reduced. They obtained Strouhal number values in the range of 0.6 to 1 depending mainly on the R ratio and slightly on the Reynolds number. For a given jet velocity (Reynolds number), they observe that the Strouhal number increases with increasing R for $R < 3.5$, and decreases for higher R values.

In our study, the probe location was determined from the visualization in order to detect the vortex passage. Consequently, as shown in Fig. 8, the position depends on the R ratio. For $R = 2$ the probe was put in a plane including the jet and the pipe axis, 6.5 mm from the wall and 1 mm downstream of the jet axis. For the $R = 4$ ratio, this probe was now placed in the same plane and at the same distance from the wall but 3 mm upstream of the jet axis. In the two cases this probe location corresponds to the upstream side of the jet. Values obtained indicate that the Strouhal number decreases as the jet velocity (or the Reynolds number Re_{jets}) increases (Fig. 10). Nevertheless, it seems that the jet Reynolds number is not the defining parameter. When they used the same Reynolds number, Kelso et al. [6] obtained much smaller values. The Reynolds numbers Re_j considered in the Megerian and Karagozian [16] and Megerian et al. [17] studies are low compared with our case. Nevertheless, their Strouhal number values are of the same order of magnitude.

The wake vortices have the same origin as the alternate vortices observed downstream of a bluff body (Von Karman Street).
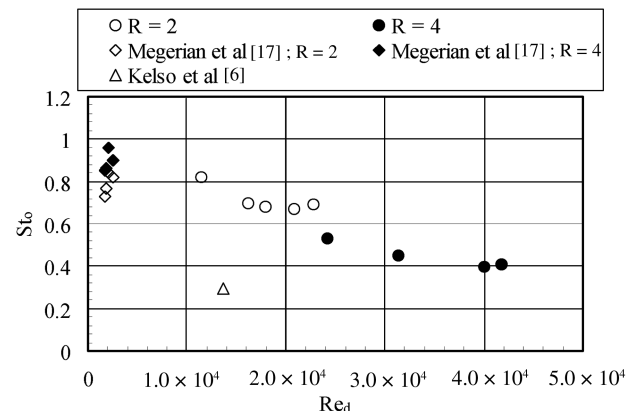

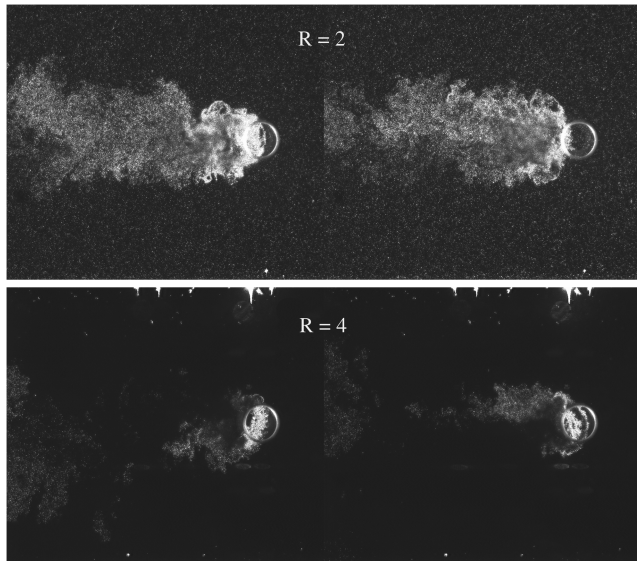**Fig. 10 Strouhal number values obtained in the jet shear layer.**

Fig. 11 Wake-type structures visualized in a longitudinal plane parallel to the pipe axis 6 mm from the wall.

Nevertheless, some authors (Fric and Roshko [5], Yuan et al. [8]) underline that the analogy is not strictly valid. A detailed analysis indicates that the vorticity associated with these transverse structures has its origin in the boundary layer developing on the wall surface.

Some separation events appear due to the positive pressure gradient existing downstream of the jet. These events provoke the creation of transverse vortices (Fric and Roshko [5]). Nevertheless, these structures depend on the Reynolds number and the velocity ratio R. Fric and Roshko [5] observe that the vortex shedding is more stable for an R ratio around four. Equivalent results were obtained during this study. Visualizations indicate that for the lower R ratio the vortex shedding is more or less symmetric and unstable (Fig. 11). On the contrary for $R = 4$, it becomes alternate and stable. The difference between these two regimes is no doubt due to the degree of interaction between the jet path, the wake vortices, and the separating events near the wall described by Fric and Roshko. In reality, the longitudinal views presented earlier (Fig. 8) indicate that in the $R = 2$ case, the jet is confined near the wall. As a result, the flapping movement of the jet described previously occurs in the flow region where the wake vortices appear. In the $R = 4$ case, the jet path is further detached from the wall, and this interaction is less important.

Fric and Roshko [5] made a detailed analysis of the characteristic frequencies associated with wake-type structures. They studied the evolution of the Strouhal number with respect to the velocity ratio and the Reynolds number. As mentioned previously they observed that the repeatability of the results is greater for velocity ratios around four. In our study the Strouhal number is based on the bulk velocity of the main flow ($St_o = f \cdot d/U_0$). Note that for the jet in crossflow (JICF) it is significantly lower than for a cylinder (0.21 for a cylinder and 0.13 for JICF). In our study, signal analyses for $R = 4$ and different upstream velocities give a constant Strouhal number of 0.11.
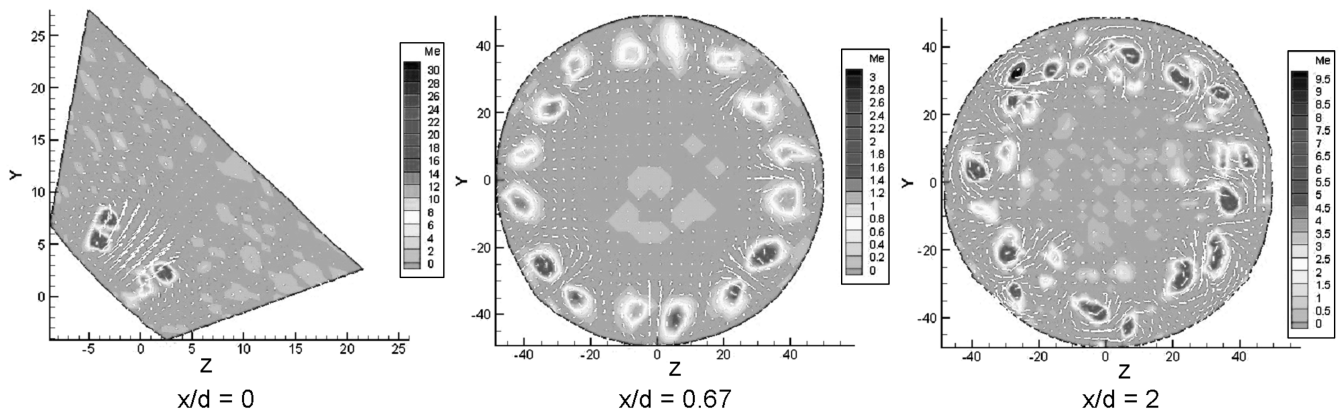

Fig. 12 Instantaneous velocity field measured by the PIV technique.
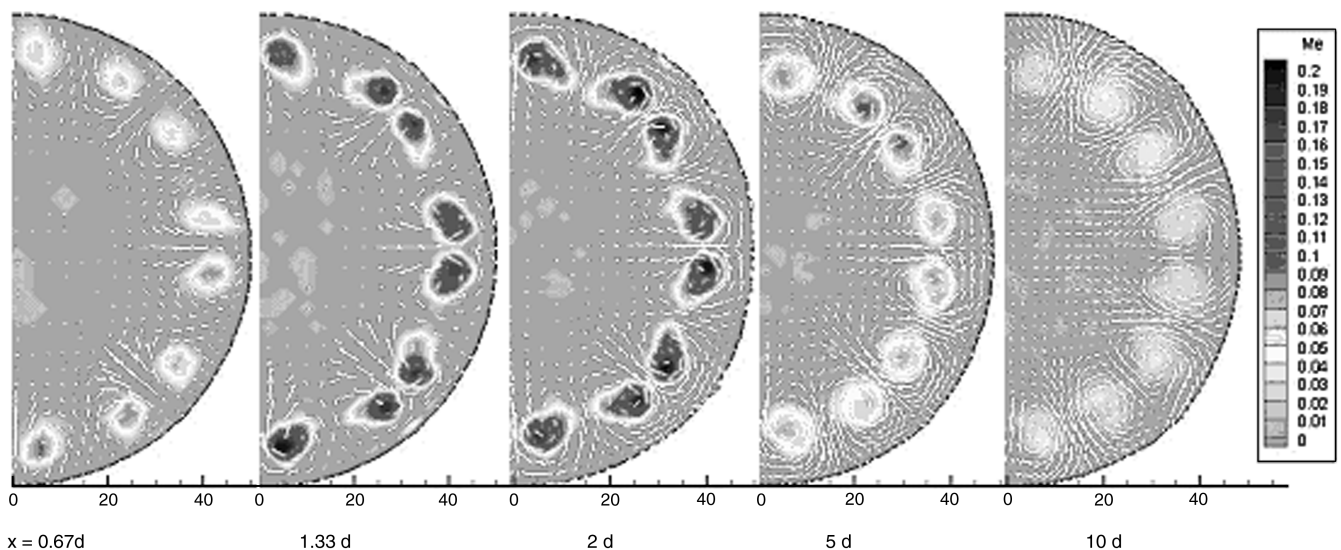

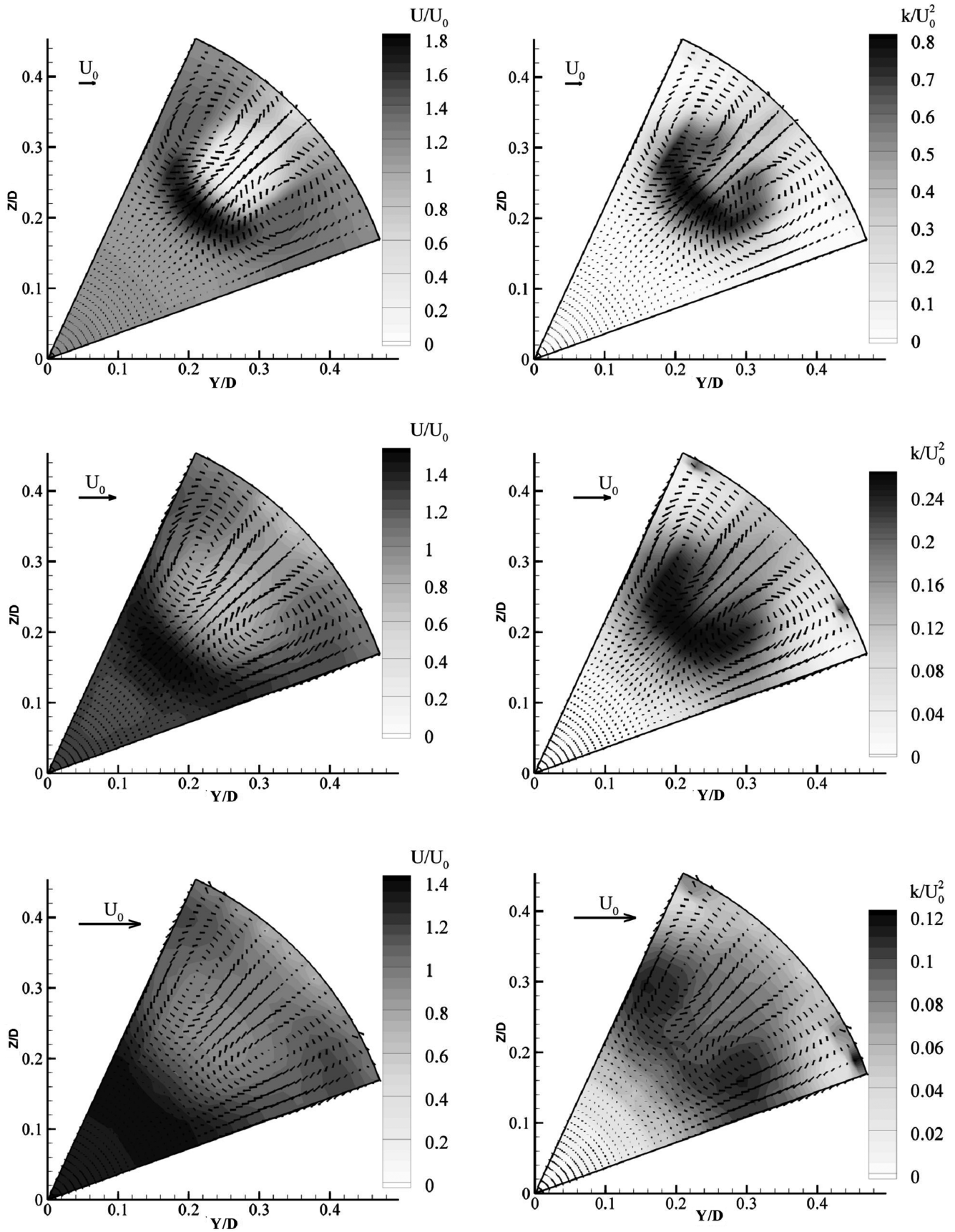**Fig. 13 Average fields obtained from PIV measurements ($R = 4$).**

Fig. 14 Mean velocity and turbulence fields measured by LDA ($R = 4$).

Velocity Field

Instantaneous fields obtained in different cross sections for $R = 4$ are plotted in Fig. 12. For $x/d = 0$, a close-up of one jet exit is presented. The vectors are the projection of the velocity on the cross section. The color scale corresponds to the amplitude of an operator "Me" exhibiting the intensity of the vorticity associated with structures present in the flow (Jeong and Hussain [27]). It is calculated from the local velocity gradients.
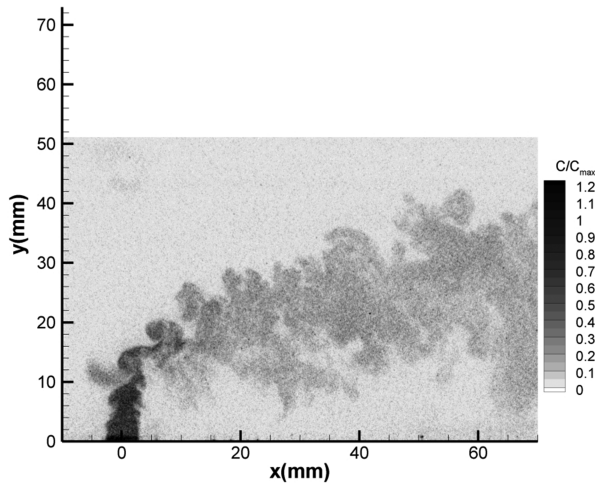
Fig. 15 Instantaneous concentration field measured by PLIF ($R = 4$).

$Me = \sqrt{H(-\Lambda_2)}$ here is equal to

$$\Lambda_2 = \frac{1}{2}\left(\left(\frac{\partial u}{\partial x}\right)^2 + \left(\frac{\partial v}{\partial y}\right)^2 + 2\frac{\partial u}{\partial y}\frac{\partial v}{\partial x}\right)$$

and H is the Heaviside step function defined by

$$H(\alpha) = \alpha \quad \text{if } \alpha > 0 \quad \text{and} \quad 0 \text{ otherwise}$$

On the first cross section ($x = 0d$), the injection velocity between two time steps is quite constant close to the wall but varies further inside the pipe. Further downstream, counter-rotative vortices are observed. The jets become more unstable, and great oscillations of the vortices are clearly seen. The interaction between two adjacent jets can be also observed. Nevertheless, this phenomenon was not studied in detail. Averaged fields plotted in Figs. 13 and 14 indicate that, even if instantaneously the twin structures are mostly asymmetrical for each jet, they become symmetrical on average. Their intensity increases close to the jet exit (Fig. 13) then decreases further downstream through diffusion effects. In Fig. 14, the characteristic kidney shape of axial velocity distribution is observed. If we compare the k distribution with the U isocontours, we note that the maximum k intensities are located in the steep velocity gradient region at the outer edge of the jet and the wall. The maximum k intensity reaches $0.74U_o^2$ ($0.046U_{jet}^2$) $2d$ from the jet outlets and decreases dramatically further downstream; $0.24U_o^2$ ($0.015U_{jet}^2$) at $5d$ and $0.11U_o^2$ ($0.0069U_{jet}^2$) at $10d$. The magnitude of k is quite high in the wake of the jet due to the velocity fluctuations generated by the wake vortices. At $10d$ from the jet outlets, the k isocontours divide into two discrete lobes, each corresponding to a vortex of the counter-rotating vortex pair.

Concentration Field

The instantaneous concentration fields shown in Fig. 15 exhibit the jet deflection and the shear layer vortices observed from Mie visualizations. Further downstream the jet is seen to spread towards the pipe axis and the wall. From a set of 100 instantaneous images, it is possible to calculate the mean and rms distributions of acetone vapor (Fig. 16).[‡] On these figures, we observe the potential core close to the jet outlet and the tracer diffusion further downstream. The rms isovalues exhibit the potential core and the high-level zone linked to the shearing at the jet boundary. From these fields it is possible to obtain radial profiles of the averaged concentration in different pipe sections and to extract the averaged trajectory and the envelope of the jets (Fig. 17). The trajectory path corresponds to the y coordinate y_{max} where the maximum of concentration is reached on each x line. The

---

[‡]The gray artifact appearing on the windward side of the jet is due to the interaction between an unwanted laser sheet reflection and the seeded jet located behind the jet under investigation.
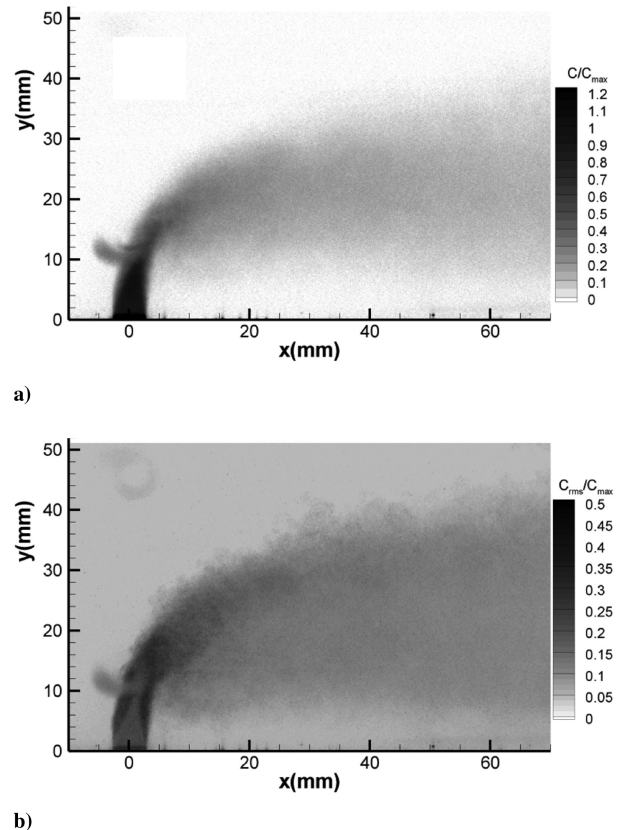

a)

b)

Fig. 16 Graphs showing a) mean, and b) rms concentration field measured in a plane perpendicular to the wall including the jet axis ($R = 4$).
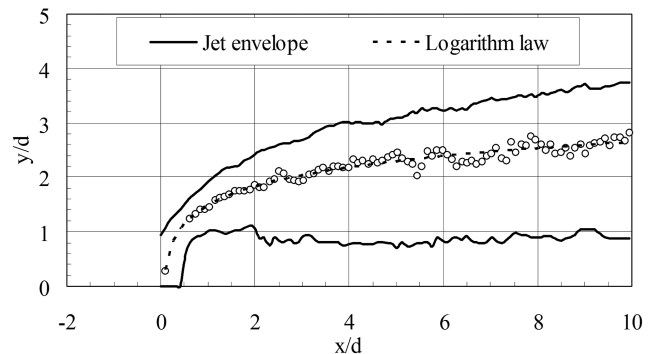

Fig. 17 Jet trajectory and envelope deduced from concentration fields ($R = 2$; $Re = 3.3 \times 10^4$).

jet envelope is characterized by a parameter b, which is defined on each radial profile by

$$b(x) = |y_{1/2}(x) - y_{max}(x)|$$

In this expression, $y_{1/2}(x)$ are the y coordinates on both jet sides where the concentration is equal to half the maximum concentration. The flow being asymmetric, two b scales are calculated, b_{in} toward the pipe axis and b_{out} toward the wall. Note that in these calculations, the x and y origins are set at the jet exit in its center. The jet penetration and its spreading depend on the R ratio (Fig. 18). For $R = 2$ and 4, the jet penetrates $2d$ and $4d$ from the wall, respectively. The spreading length ($b_{in} + b_{out}$) increases with the R ratio (2.8d and 3.9d, respectively, for $x/d = 10$). If we compare the average trajectories deduced from the velocity or the concentration fields, we notice discrepancies (Fig. 18). The velocity profiles give higher penetration rates than the concentration field. Equivalent results were obtained experimentally by Kamotani and Greber [18] and Patrick [19] and more recently by Su and Mungal [10] or from LES
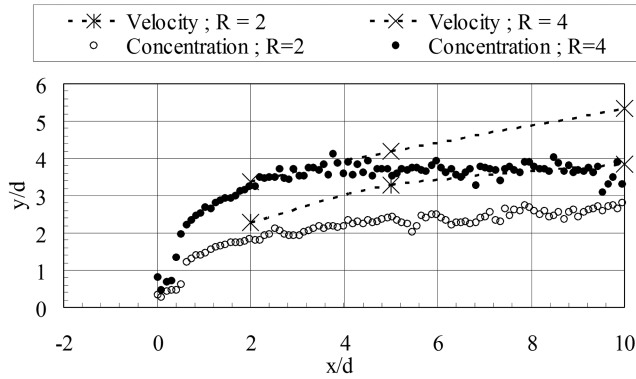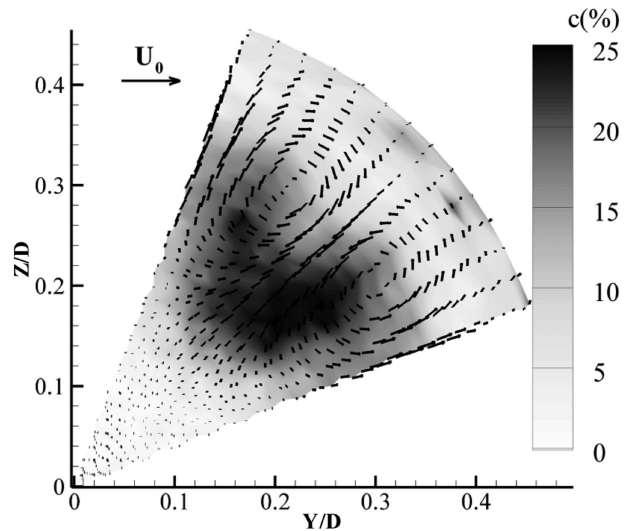
Fig. 18   Comparison between the jet trajectories deduced either from the velocity or from the concentration fields.

simulations by Prière et al. [15]. A comparison between velocity and concentration fields (Fig. 19) may explain this difference. In fact, it indicates that the tracer is concentrated at the periphery of the two twin vortices above the high velocity zone.

a)
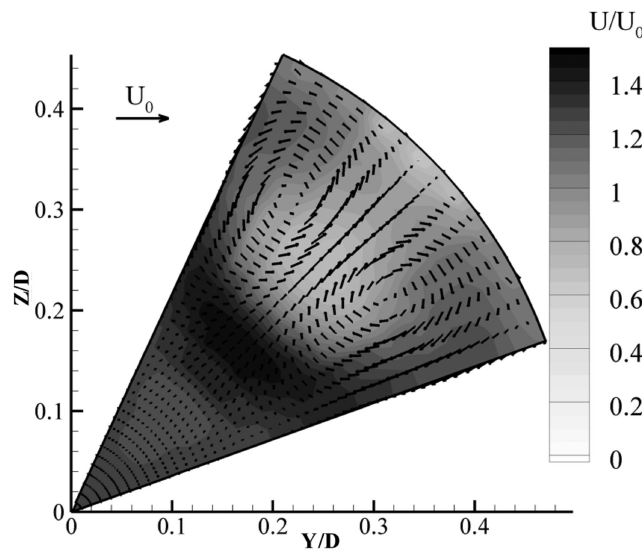
b)

Fig. 19   Comparison of the averaged velocity and concentration fields ($R = 4$; $x/d = 5$) showing a) color: concentration, vector: transverse velocity components from PIV; and b) color: axial velocity component, vector: transverse velocity components from LDA.

To complete this analysis, the results obtained for the two R ratios are compared by scaling the spatial coordinate by the product $R.d$ previously used by Pratte and Baines [3], Smith and Mungal [7], and Su and Mungal [10] (Fig. 20). The jet trajectory obtained by Su and Mungal [10] and Pratte and Baines [3] are in good accordance. The penetration distance found by Smith and Mungal [7] is appreciably less than those obtained in the two other studies. Su and Mungal [10] explained that this difference can be linked to the jet exit velocity profile used in the two studies. Smith and Mungal [7] used a top-hat jet exit velocity profile similar to the one used in this study, whereas Su and Mungal [10] used a pipe flow profile. The same behaviors were observed by Muppidi and Mahesh [20] and New et al. [21]. The jet trajectories obtained in the present study indicate an influence of the confinement, which imposes a quicker bending of the jets. Despite this difference, this scaling is useful for collapsing the trajectory for x/Rd values below 1.2. For higher x/Rd values, the jet penetration is effectively stopped (i.e., the penetration distance is constant) for $R = 4$, whereas the jet continues to penetrate for all downstream locations for $R = 2$.

In Fig. 17, we observe that the jet spreads more quickly toward the jet wall than toward the axis. In Fig. 21, the spreading rate in the two directions is analyzed through the b parameter introduced before. A similitude is obtained close to the jet outlet using the scaling parameter Rd especially toward the axis. In the other direction, when
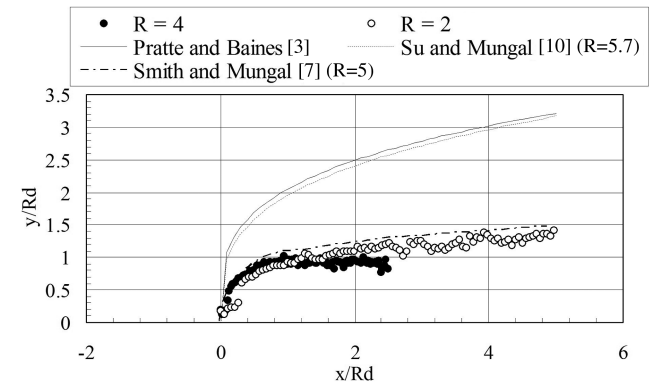

Fig. 20   Jet trajectories deduced from concentration fields ($Re = 3.3 \times 10^4$).
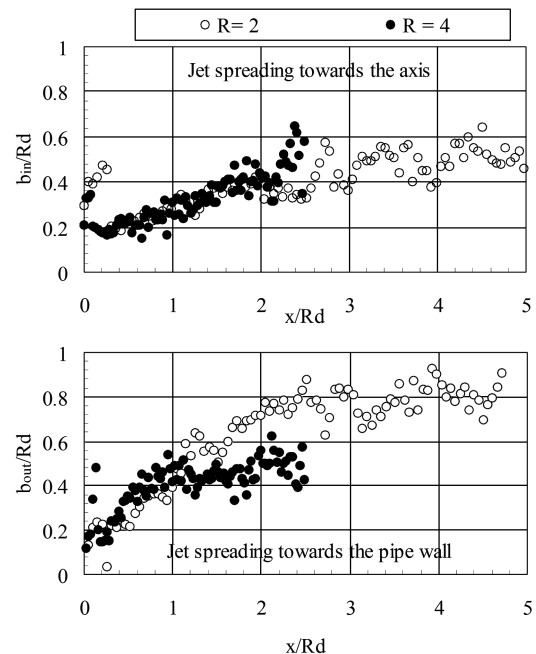

Fig. 21   Jet spreading characteristics along the jet path ($Re = 3.3 \times 10^4$).

comparing the spreading rate for the two R ratios, we observe that for x/Rd values above 1.2, the jet expansion is inferior for $R = 4$. This observation can be linked to the jet trajectory curves plotted in Fig. 20 where we notice that the deviation between the two trajectories appears at the same x/Rd coordinate. It seems that in the $R = 4$ case, the confinement of the jets imposes a greater deviation of the jet toward the wall. In consequence, the jet spreading in this direction diminishes as shown in Fig. 21.

To analyze the shape of the concentration profile, the concentration levels are normalized by the maximum concentration obtained on each profile. For the x coordinate, the distance from the location of the maximum normalized by the b length scale is used. The results plotted in Fig. 22 show that a self-similarity is obtained, which can be described by a Gaussian law:

$$\frac{C}{C_{max}} = e^{-0.6931(\frac{y-y_{max}}{b})^2}$$

Similar results were obtained by Smith and Mungal [7]. Nevertheless, these authors note that the self-similarity in the two orthogonal directions is not reached for $x/rd < 5$.
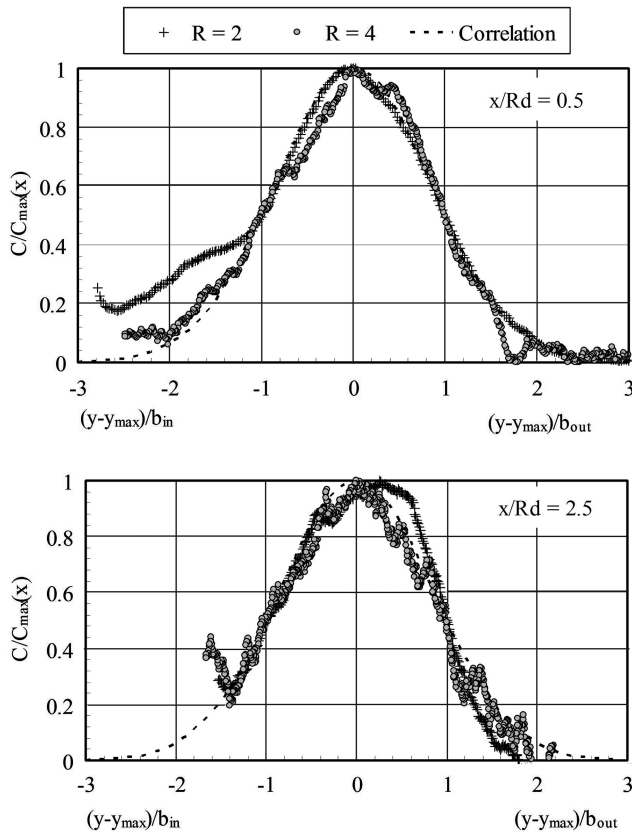

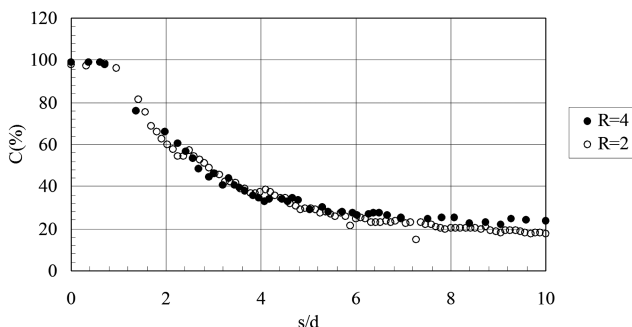**Fig. 22   Concentration profiles ($Re = 3.3 \times 10^4$).**

Fig. 23   Maximum concentration decrease along the jet path ($Re = 3.3 \times 10^4$).

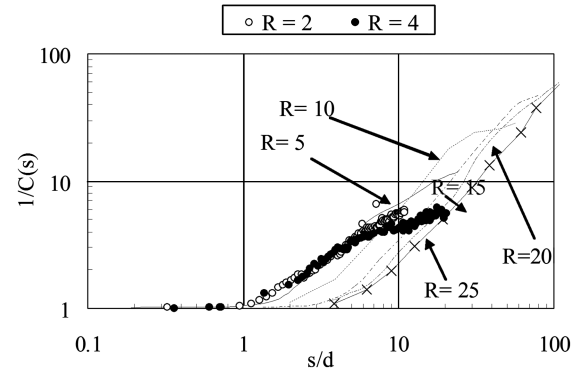**Fig. 24   Maximum concentration intensity along the jet trajectory ($Re = 3.3 \times 10^4$), where curves correspond to Smith and Mungal [7] results.**
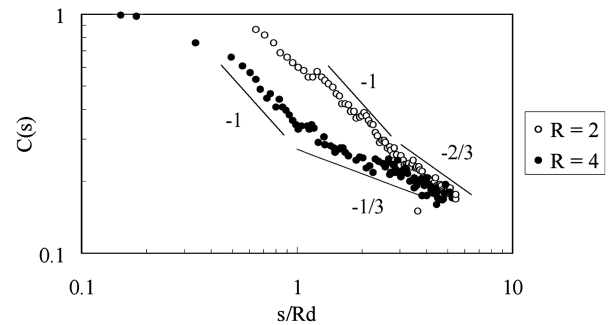

Fig. 25   Maximum concentration decay plotted with distance s normalized by Rd.

From the paths, it is possible to calculate the curvilinear abscissa along the jet trajectory, that is, the distance traveled along the jet trajectory from the injection point (denoted here by s). When the concentration distribution is plotted along this parameter (Fig. 23), two regions are observed: close to the jet exit, the potential zone where the concentration remains constant and further downstream the diffusion zone characterized by a decrease of the concentration level. The length of the potential region is equal to $1d$.

If the inverse of the concentration level is plotted with respect to the curvilinear abscissa s/d (Fig. 24), a unique distribution is obtained for the two R ratios, which indicates that the concentration decay depends only on the distance from the jet outlet. Such behavior was also observed on the velocity decrease along the jet axis for free jets. Nevertheless, this behavior was not obtained by Smith and Mungal [7]. When we plot our results in the form proposed by these authors (Fig. 25), that is, in log–log coordinates with the s/Rd parameter, we obtain a slope that depends on the R ratio. For $R = 2$, the concentration decay follows first an s^{-1} law then $s^{-2/3}$. A same tendency in the far field was observed by Smith and Mungal [7]. For $R = 4$, the concentration decrease begins in s^{-1} and continues in $s^{-1/3}$. The behavior observed for this R value may be linked to the observations done previously from Figs. 20 and 21. As highlighted before for $R = 4$, the confinement imposes a greater bending of the jets, which limits their spreading toward the wall and globally induces a lower decay of the acetone concentration as shown in Fig. 25.

Conclusions

The mixing of eight jets flowing transversally into a pipe flow are studied using different experimental techniques in order to reveal unsteady and steady features of the flow. A detailed data bank is obtained that can be used to validate numerical simulations performed with RANS, URANS, or LES codes.

This study confirms some previous results obtained on JICF configurations. In particular, the behaviors of different vortical structures are similar to the description given by Fric and Roshko [5].

Spectral analyses on wake structures confirm the results obtained by these authors especially concerning the influence of the R ratio on the signal-to-noise ratio. The analyses performed on the shear layer structures are in good agreement with the observations of Megerian et al. [17]. Nevertheless, it seems that new studies are needed to improve the understanding of the behavior of these shear layer structures at the Reynolds number range considered in this study.

The comparison between the velocity and concentration fields indicates that the tracer is concentrated between the two twin vortices' location and the bean-shaped high-velocity zone. This result confirmed the difference in the jet trajectories deduced either from the velocity or the concentration fields. Close to the jet outlets, the PLIF results confirm that the different concentration fields can be characterized by the nondimensional length $R.d$ introduced by Pratte and Baines [3]. Further downstream, comparisons between the two R ratios indicate that a confinement effect appears when this parameter is increased. This effect augments the deviation of the jets in the crossflow direction and modifies the jet expansion toward the wall, and finally the concentration decrease.

Acknowledgments

References

[1] Poinsot, T., and Veynante, D., *Theoretical and Numerical Combustion*, R. T. Edwards, Inc., Flourtown, PA, 2005.

[2] Margason, R. J., "Fifty Years of Jet in Crossflow Research, In Computational and Experimental Assessment of Jets in Crossflow," AGARD CP-534, Winchester, UK, 1993.

[3] Pratte, B. D., and Baines, W. D., "Profiles of Round Turbulent Jets in Cross Flow," *Journal of Hydraulic Division, Proceedings of the American Society of Civil Engineers*, Vol 92, 1967, pp. 53–64.

[4] Werlé H., "Flows with Very Large Velocity Fluctuations," *Motion Picture Film n° 575*, ONERA, Chatillon, France, 1968.

[5] Fric, T. F., and Roshko, A., "Vortical Structure in the Wake of a Transverse Jet," *Journal of Fluid Mechanics*, Vol. 279, 1994, pp. 1–47.
doi:10.1017/S0022112094003800

[6] Kelso, R. M., Lim, T. T., and Perry, A. E., "An Experimental Study of Round Jets in Cross flow," *Journal of Fluid Mechanics*, Vol. 306, 1996, pp. 111–144.
doi:10.1017/S0022112096001255

[7] Smith, S. H., and Mungal, M. G., "Mixing, Structure and Scaling of the Jet in Cross flow," *Journal of Fluid Mechanics*, Vol. 357, 1998, pp. 83–122.
doi:10.1017/S0022112097007891

[8] Yuan, L., Street, R., and Ferziger, J. H., "Large Eddy Simulation of a Round Jet in Cross-Flow," *Journal of Fluid Mechanics*, Vol. 379, 1999, pp. 71–104.
doi:10.1017/S0022112098003346

[9] Lim, T. T., New, T. H., and Luo, S. C., "On the Development of Large-Scale Structures of a Jet Normal to a Cross Flow," *Physics of Fluids*, Vol. 13, No. 3, 2001, pp. 770–775.
doi:10.1063/1.1347960

[10] Su, L. K., and Mungal, M. G., "Simultaneous Measurements of Scaler and Velocity Field Evolution in Turbulent Crossflowing Jets," *Journal of Fluid Mechanics*, Vol. 513, 2004, pp. 1–45.
doi:10.1017/S0022112004009401

[11] Holdeman, J. D., "Mixing of Multiple Jets with a Confined Subsonic Cross flow," *Progress in Energy and Combustion Sciences*, Vol. 19, No. 1, 1993, pp. 31–70, doi:10.1016/0360-1285(93)90021-6.

[12] Holdeman, J. D., Liscinsky, D. S., Oechsle, V. L., Samuelsen, G. S., and Smith, C. E., "Mixing of Multiple Jets with a Confined Subsonic Crossflow: Part I—Cylindrical Duct," *Journal of Engineering For Gas Turbines and Power*, Vol. 119, No. 4, 1997, pp. 852–862.
doi:10.1115/1.2817065

[13] Leong, M. Y., Samuelsen, G. S., and Holdeman, J. D., "Mixing of Jet Air with a Fuel Rich Reacting Cross flow," *Journal of Propulsion and Power*, Vol. 15, No. 5, 1999, pp. 617–622.
doi:10.2514/2.5479

[14] Blomeyer, M. K., Krautkremer, B., Hennecke, D. K., and Doerr, T., "Mixing Zone Optimization of a Rich-Burn/Quick-Mix/Lean-Burn Combustor," *Journal of Propulsion and Power*, Vol. 15, No. 2, 1999, pp. 288–295.
doi:10.2514/2.5425

[15] Prière, C., Gicquel, O., Gajan, P., Strzelecki, A., Poinsot, T., and Berat, C., "Experimental and Numerical Studies of Dilution Systems for Low-Emission Combustors," *AIAA Journal*, Vol. 43, No. 8, 2005, pp. 1753–1766.
doi:10.2514/1.14681

[16] Megerian, S., and Karagozian, A., "Evolution of Shear Layer Instabilities in the Transverse Jet, Reno," AIAA Paper 2005-142, 2005.

[17] Megerian, S., Davitian, J., Alves, B., and Karagozian, A., "Transverse-Jet Shear Layer Instabilities. Part 1. Experimental Studies," *Journal of Fluid Mechanics*, Vol. 593, 2007, pp. 93–129.doi:10.1017/S0022112007008385

[18] Kamotani, Y., and Greber, I., "Experiments on a Turbulent Jet in a Crossflow," *AIAA Journal*, Vol. 10, No. 11, 1972, pp. 1425–1429.
doi:10.2514/3.50386

[19] Patrick, M. A., "Experimental Investigation of the Mixing and Penetration of a Round Turbulent Jet Injected Perpendicularly into a Transverse Stream," *Chemical Engineering Research and Design* , Vol. 45a, 1967, pp. 16–31.

[20] Muppidi, S., and Mahesh, K., "Study of Trajectories of Jets in Crossflow Using Direct Numerical Simulations," *Journal of Fluid Mechanics*, Vol. 530, 2005, pp. 81–100.
doi:10.1017/S0022112005003514

[21] New, T. H., Lim, T. T., and Luo, S. C., "Effects of Jet Velocity Profiles on a Round Jet in Cross-Flow," *Experiments in Fluids*, Vol. 40, No. 6, 2006, pp. 859–875.
doi:10.1007/s00348-006-0124-y

[22] Lourenço, L., and Krothapalli. A., "True Resolution PIV: A Mesh-Free Second Order Accurate Algorithm," *10th International Symposium on Applications of Laser Techniques in Fluid Mechanics*, Lisbon, 2000.

[23] Raffel, M., Willert C., and Kompenhaus, J., "Particle Image Velocimetry : A Practical Guide," Springler–Verlag, New York, 1998.

[24] Hanson, R. K., Seitzman, J. M., and Paul, P. H., "Planar Laser-Fluorescence Imaging of Combustion Gases," *Applied Physics. B, Lasers and Optics*, Vol. 50, No. 6, 1990, pp. 441–454.
doi:10.1007/BF00408770

[25] Batchelor, G. K., "Small Scale Variation of Convected Quantities Like Temperature in Turbulent Fluid: Part I," *Journal of Fluid Mechanics*, Vol. 5, 1959, pp. 113–133.
doi:10.1017/S002211205900009X

[26] Batchelor, G. K., "Small Scale Variation of Convected Quantities Like Temperature in Turbulent Fluid: Part II," *Journal of Fluid Mechanics*, Vol. 5, 1959, pp. 134–139.
doi:10.1017/S0022112059000106

[27] Jeong, J., and Hussain, F., "On the Identification of a Vortex," *Journal of Fluid Mechanics*, Vol. 285, 1995, pp. 69–94.
doi:10.1017/S0022112095000462

N. Clemens
Associate Editor